Cu/Ag–Sb–I Rudorffite Thin Films for Photovoltaic Applications

Rik Hooijer, Andreas Weis, Waldemar Kaiser, Alexander Biewald, Patrick Dörflinger, Clément Maheu, Oleksandr Arsatiants, David Helminger, Vladimir Dyakonov, Achim Hartschuh, Edoardo Mosconi, Filippo De Angelis, Thomas Bein*

Abstract

In the search for lead-free perovskites, silver pnictohalides recently gained attention as novel perovskite-inspired materials for photovoltaics due to their high stability, low toxicity, and promising early efficiencies, especially for indoor applications. Recent research on such “rudorffites” mainly addresses silver bismuth iodides (Ag–Bi–I), while their antimony analogues are hardly investigated due to intrinsic challenges in the synthesis of Sb-based thin films. Here, we establish a synthetic route to prepare Ag–Sb–I thin films by employing thiourea as a Lewis-base additive. Thin film morphologies were further optimized by alloying them with Cu, resulting in solar cells with an improved power conversion efficiency of 0.7% by reducing undesired side phases. Density functional theory calculations and optical characterization methods support the incorporation of Cu into a $Cu_{1-x}Ag_xSbI_4$ phase, keeping the overall stoichiometry and band gap virtually unchanged upon alloying. Our results further reveal the detrimental role of Ag point defects representing trap states in the band gap, being responsible for low open-circuit voltages and subgap absorption and emission features. Moreover, additional minor amounts of Bi are shown to boost the efficiency and stabilize the performance over a wider compositional range. Despite the remaining challenges regarding device performance, we demonstrate a strong increase in external quantum efficiency when reducing the light intensity, highlighting the potential of Ag–Sb–I rudorffites for indoor photovoltaics.

Published as part of *Chemistry of Materials* virtual special issue “ In Honor of Prof. Clement Sanchez”.

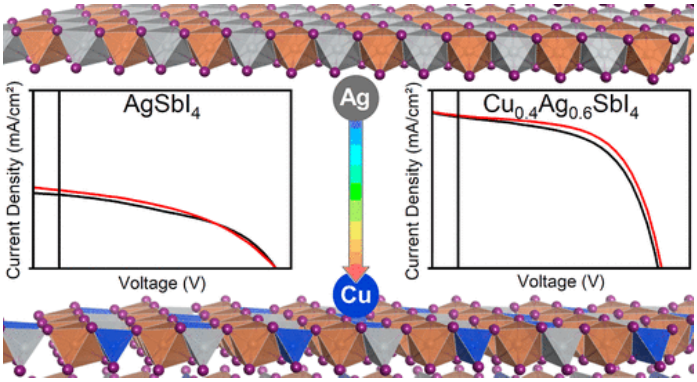

Introduction

Lead-halide perovskites have drawn enormous interest for optoelectronic applications, particularly photovoltaics, from industry and research alike. Still, the practical applications of these materials remain limited by their notorious instability coupled with the high toxicity of the constituents and degradation products. (1−4) Nonetheless, through the recent upsurge of emerging semiconducting materials, the focus of photovoltaic research has greatly shifted from purely inorganic materials, such as silicon or CIGS (Cu–In–Ga–Se), with high energy demands for production, to novel compounds that combine favorable optoelectronic properties with remarkable defect tolerance in combination with low-temperature solution syntheses. (5−9)

Starting from the prototypical methylammonium lead iodide, $MAPbI_3$, a classical strategy to circumvent the toxicity issues is homovalent or heterovalent substitution of the central lead atom while retaining the perovskite structure. This is commonly achieved through elements with the same ns^2 electronic configuration as this was repeatedly suggested to be the basis of the exceptional defect tolerance in lead-halide perovskites. (10−12) An obvious and intensely studied candidate for substitution is the group IV neighbor tin, which was shown to be both efficient and less problematic than lead in terms of environmental impact. (13,14) Nonetheless, $MASnI_3$ and other Sn(II)-based compounds are highly sensitive toward oxidation, requiring pure precursor chemicals and nonoxidizing solvents, which still hampers the successful implementation of these materials. (15−18) Alternative approaches combine adjacent elements of tin and lead in the periodic table, namely, trivalent antimony(III) and bismuth(III), which still showcase the characteristic electronic ns^2 configuration, with monovalent cations like silver and copper, as prominently seen and studied in the archetype double-perovskite $Cs_2AgBiBr_6$. (19,20) Although this compound exhibits several promising properties, like a long charge carrier lifetime and high environmental stability, its photovoltaic efficiency is limited by rapid nonradiative recombination and a large band gap. (19−21)

If the monovalent metal ion is omitted entirely in the above systems, the original perovskite structure is sacrificed, leading to another class of perovskite-derived materials with the general structural formula $A_3B_2X_9$, which also suffer from detrimental factors such as high exciton binding energies, strong exciton–phonon coupling, low dimensionality, and others. (22−25) Herein, the A-site cations are mostly derived from the lead-based perovskite counterparts, namely, methylammonium, formamidinium, or cesium(I). Many reports have already shown the significant influence of these cations, not only on the electronic properties but also as structure-directing agents. (26,27)

Most recently, a new class of Sb/Bi-based materials has emerged, with the accompanying monovalent A cations being silver and/or copper, featuring the general structural formula $A_xB_yX_{x+3y}$ and straying even further from the original perovskite lattice. These compounds were termed “rudorffites” (28) in previous reports and are composed of interconnected $[A/B]X_6$ octahedra, where the A and B cations share equivalent lattice positions, thereby inducing a high degree of stoichiometric freedom. Notably, these pnictohalides show favorable band gaps for single-junction solar cell devices and high absorption coefficients. (28,29) The hitherto published materials are mostly based on Ag–Bi–I and were shown to already surpass 5% PCE within only a couple of years’ time. (30) Moreover, rudorffites were also employed successfully in other types of devices like X-ray detectors, (31) memristors, (32) or recently as highly efficient indoor light harvesters, (33,34) competing with commercial solar cells in this field. Alloying and substituting Ag with Cu were also shown to be efficient ways to tailor their structural and electronic properties. (33,34)

While research efforts to date have been mostly focused on Bi-based rudorffite structures, only a few reports concerning pure (Ag/Cu)–Sb–I materials can be found, some of which being inconclusive about important properties like color, band gap, and structure. (35,36) This may be due to synthetic difficulties when working with SbI_3 as a precursor, (37) which exhibits a high vapor pressure and is prone to evaporation when using film annealing temperatures above 100 °C. Furthermore, instability of the pristine $AgSbI_4$ under ambient conditions was reported as well. (38)

Herein, we demonstrate the thin-film synthesis of $Cu_xAg_{1-x}SbI_4$ (CASI) rudorffites using a Lewis-base-assisted approach. We establish the formation of the crystalline materials in thin films and furthermore, we highlight the beneficial effect of an optimal ratio of 40% Cu to Ag on the morphology, reducing grain boundaries, and improving the overall coverage. Notably, substitution of Sb with only 5% of Bi led to a further morphology improvement over a broader range up to a Cu content of 90%, which can also be seen in the photovoltaic performance. Density functional theory (DFT) calculations investigate the impact of the stoichiometry of various (Cu/Ag)–Sb–I phases, highlighting the incorporation of Cu into the layered CASI composition. X-ray photoelectron spectroscopy measurements demonstrate the disappearance upon Cu addition of other trivalent oxide or metallic antimony states like SbO_x, SbI_3, and Sb^0 as side phases likely created through degradation and surface oxidation. UV–vis spectroscopy and photoluminescence (PL) measurements further reveal the presence of deep defect states and broad emission with a large Stokes shift, confirmed by DFT calculations pointing to extraordinarily low Ag point defect formation energies of 0.16 eV. Additionally, PL measurements reveal static emission and lifetime characteristics over the whole doping range, which we discuss in view of varying charge carrier mobilities and photovoltaic performance. Conceptually, we connect the luminescence behavior to the thin film morphology via hyperspectral optical measurements, explaining the improved performance in solar cells with an optimal Cu content. Lastly, external quantum efficiency measurements reveal a much-improved photocurrent at low photon flux when no white light bias is employed, indicating the great potential of these materials for indoor photovoltaic applications.

Results and Discussion

To synthesize thin films based on CASI, a common approach was employed by dissolving the corresponding halide precursors ($CuI/AgI/SbI_3$) in a 1:1 DMF/DMSO mixture to achieve a concentration of 0.6 M, followed by spin-coating on different substrates (glass/FTO/ITO/mp-TiO_2). Furthermore, a small amount of the Lewis-base thiourea (TU) was added to retard the crystallization of the thin film, a crucial step in controlling the formation of the CASI material, which has been reported to exhibit significant formation issues. (36,38,39) This is a necessary step to obtain working devices and circumvent recurrent problems of the halide precursors, with AgI being only hardly soluble in organic solvents such as DMF that are commonly used for spin-coating. The influence of the additive on the behavior of the precursor solution is presented in Figure S1 in the Supporting Information. Similar effects have been shown for lead-based and lead-free perovskites. (40−43) Furthermore, SbI_3 is known to have a high equilibrium vapor pressure (37) which prohibits the use of elevated annealing temperatures and is shown to be crucial for the formation of the Bi analog. (29) In this work, we therefore employed a ramped thermal annealing approach from 50 °C for 1 h to 80 °C for 1 min, to anneal the films. An “inverse” technique based on one short immediate heating step for 1 min at 120 °C leads to improved crystallinity but less complete coverage, as shown in the XRD graphs and SEM images in Figure S3.

Materials based on $A_xB_yI_{x+3y}$ stoichiometries, with A being a monovalent transition metal cation (Ag^+/Cu^+) and B being a trivalent pnictogen cation (Bi^{3+}/Sb^{3+}), are constructed of alternating occupied and unoccupied positions of edge-sharing octahedra $[AI_6]^{5-}$, $[BI_6]^{3-}$, and $[\Delta X_6]^{6-}$ (Δ = vacancy). (39) By maintaining the edge-sharing octahedral lattice and the charge neutrality through vacancies, the entire A–B–I phase space can be defined. (28) $AgSbI_4$ and Ag_3SbI_6 are the most reasonable structural models based on space group $R\overline{3}m$ (no. 166) as more Sb-rich phases have very high formation energies and very small band gap energies around 0.4 eV, as discussed later based on DFT calculations. Because of the aforementioned disorder, exact crystal structure analysis of such materials was shown to be a challenge, especially since the diffraction patterns are extremely similar and different symmetry groups with partial positional occupations can produce satisfactory crystal structure and profile refinements. (28,39,45−49) Furthermore, for Ag- or Cu-rich compositions, the monovalent A cations may occupy the 3b positions in-between the octahedral slabs. (39,49) Our DFT calculations discussed below show slightly preferential formation of the 1:1:4 composition rather than the 3:1:6 composition, which both, however, appear to be metastable. Also, large losses in V_{oc}, as discussed later, suggest the presence of imperfect phases. Thus, we will limit our discussion to the 1:1:4 composition.

The diffractograms of CASI films on FTO are shown in Figure 1a for the incremental replacement of Ag with Cu in 10% steps. They match well with the theoretical patterns of $AgSbI_4$ extracted from the Bi analog $AgBiI_4$, up to a Cu-substitution of 80%, i.e., $Cu_{0.8}Ag_{0.2}SbI_4$ and $Cu_{0.9}Ag_{0.1}SbI_4$ assuming the same space group ($R\overline{3}m$) and a related crystal structure based on the $CdCl_2$ prototype, in line with Gray et al. (36,50) For the thin film of pure $AgSbI_4$ (without Cu), a significant contribution of the AgI side phase can be observed at 23.8° (Figure 1a red), which can be completely avoided with the first substitution step to $Cu_{0.1}Ag_{0.9}SbI_4$ (Figure 1a, orange). Good agreement with the theoretical structure is shown in the bottom part of Figure 1b through a profile peak refinement using the Le Bail method. Note that a profile refinement with the Ag_3BiI_6 structure results in a similar agreement (Figure S17). Interestingly, within the next two substitution steps, the relative intensity of the (101) reflection is reduced to a minimum, and for $Cu_{0.2}Ag_{0.8}SbI_4$ (light orange), a second strong reflection at 24.66° appears, which has a weak intensity and is shifted to higher angles, at 25° for $Cu_{0.3}Ag_{0.7}SbI_4$ (yellow). These reflections are absent after inclusion of 40% Cu and higher, as shown in the top part of Figure 1b for $Cu_{0.4}Ag_{0.6}SbI_4$, agreeing well with the structure of $AgSbI_4$. As the true origin of these reflections is nontrivial and would require detailed solid state and structural analysis, which is beyond the scope of this article, we suggest a few considerations. Upon substitution of Ag with Cu, we expect the octahedral coordination to be strongly distorted, as Cu^+ generally prefers tetrahedral coordination. This, along with the smaller ionic radius of Cu^+ (0.6 Å for tetrahedral coordination and 0.77 Å for octahedral coordination) compared to that of Ag^+ (1.15 Å for octahedral coordination), should lead to deformations of the octahedral symmetry and the lattice parameters, as shown below in Figure 4b, where Ag/Cu coordination was optimized to a tetrahedral coordination through DFT calculations. (51) As most reflections in the sequence of XRD patterns do not change their position as drastically as the (101) reflection, a large change in the unit cell parameters is not plausible here. The shift and the increased width of the aforementioned reflections at 24.66 and 25° further indicate the presence of overlapping reflections, which can also be observed for $Cu_{0.8}Ag_{0.2}SbI_4$ and $Cu_{0.9}Ag_{0.1}SbI_4$ for the (003), (012), and (006) reflections (see Figure 1). Since the inclusion of Cu distorts the octahedral structure, a reduction in symmetry from $R\overline{3}m$ to $C2/m$ or other lower symmetry subgroups is possible. Profile refinement using the structural solution from DFT, as discussed later, in the triclinic space group $P1$ agrees well with the observed thin film diffractogram (Figure S18). Lastly, for $Cu_{0.8}Ag_{0.2}SbI_4$ and $Cu_{0.9}Ag_{0.1}SbI_4$, the decreased crystallinity, the decreased number of observable reflections, and the appearance of a reflection at 10.48° suggest a structural breakdown and formation of a different phase than $AgSbI_4$. Consistently, the photovoltaic performance of materials with Cu contents of more than 60% is substantially reduced, as discussed below.

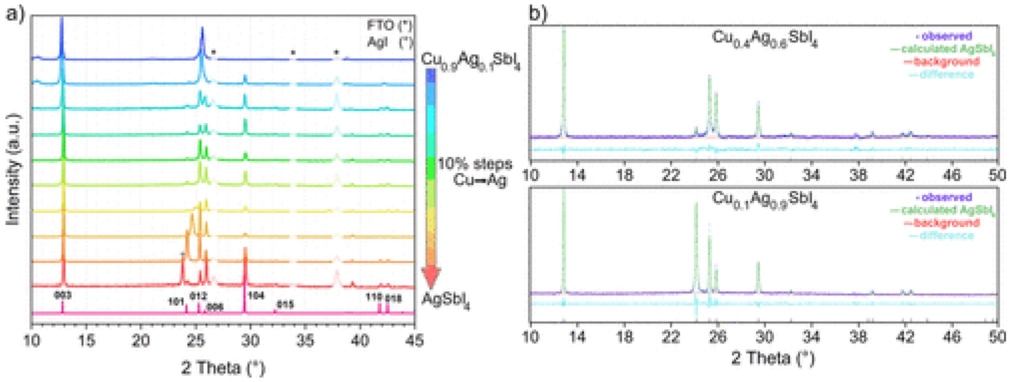

Figure 1. Thin film XRD data are normalized to the highest intensity. (a) CASI thin films on FTO substrates. Increasing Cu concentrations in steps of 10% coded from red to blue with theoretical patterns from Gray et al. (36) FTO reflections are transparent and marked with an asterisk (*). (b) Peak profile refinements with the Le Bail method for $Cu_{0.1}Ag_{0.9}SbI_4$ and $Cu_{0.4}Ag_{0.6}SbI_4$. (44)

Previous reports suggested an intrinsic instability of the $AgSbI_4$ phase, whereas the Bi-based analog with a larger ionic radius was shown to be highly stable under synthesis and in ambient conditions. (36) Moreover, Al-Anesi et al. showed local symmetry enhancement through Sb doping of Cu_2AgBiI_6, thereby improving photovoltaic efficiency through enhanced local structural symmetry and thus reducing defect density. (34) Consequently, we also prepared a system with only a small addition of 5% Bi, resulting in a decrease in band gap (discussed later) and improved morphology. The corresponding XRD patterns show no significant change when comparing Bi-alloyed structures versus pure antimony thin films (see Figure S4).

In the following, we focus on samples with 0, 40, and 60% Cu/Ag as they are exemplary for the electronic and morphological changes in this system. The SEM images of those samples, shown in Figure 2a-f, highlight the strong impact of the monovalent halide precursor on the morphology and crystallization. First of all, the addition of Bi seems to generally aid the crystallization, resulting in films with significantly better coverage and homogeneous morphologies. Enhanced lattice stability may further rationalize the increased coverage and high homogeneity at 40% Cu, resulting in overall homogeneously covered films. Beyond 50% Cu, the homogeneity decreases again.

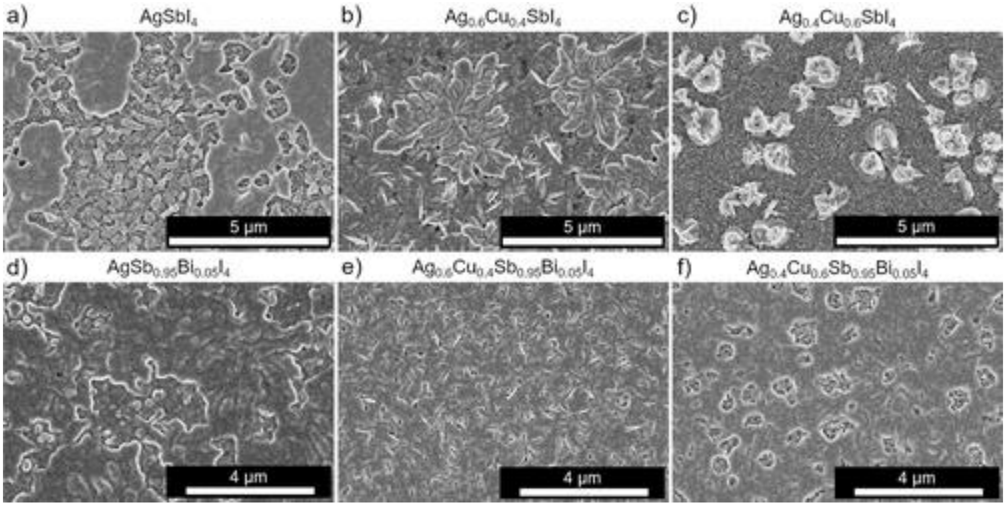

Figure 2. Scanning electron microscopy images of CASI thin films on FTO/c-TiO_2/mp-TiO_2. (a–c) Increasing amount of Cu (0, 40, and 60%) and (d–f) increasing amount of Cu (0, 40, and 60%) combined with 5% Bi/Sb-substitution.

XPS spectra confirm the incorporation of Cu and the presence of the expected elements (e.g., Ag 3d and Sb 3d), verifying the formation of the pure silver and copper-alloyed phases; see Figure S2a–c. A characteristic energy difference of 367.2 eV between Ag $3d_{5/2}$ and the VB onset was measured for the Cu–Ag–Sb/Bi–I thin films. Interestingly, the XPS spectra of the pure $AgSbI_4$ (Figure S2c) show additional states at approximately 528.7 eV (i.e., 2.0 eV below the characteristic peak of Sb^{3+}). According to the literature, it is assigned to Sb^0. (52) This side phase vanishes when Cu is added to the system (Figure S2).

We now employ a combined fitting procedure following Elliott's method for the absorption coefficient close to the band edge and Urbach tail to quantify the band gap and sub-band gap states. (53) The band gap of $AgSbI_4$ lies within the range of 2.0–2.2 eV, as in Figure 3a for $AgSbI_4$ (green), $Cu_{0.4}Ag_{0.6}SbI_4$ (blue), $Bi_{0.05}$:$AgSbI_4$ (orange), and $Bi_{0.05}$:$Cu_{0.4}Ag_{0.6}SbI_4$ (red). Changing the Cu/Ag ratio does not significantly alter the band gap, while the addition of Bi reduces the band gap by 0.2 eV. The decrease in band gap upon Bi/Sb alloying has previously been successfully assigned to the formation of aggregates rich of either Sb or Bi for similar materials, being the source of the reduction in the electronic band gap. (25,54) Furthermore, the Urbach tails all converge to the same energy of around 1.6 eV, indicating the presence of trap states. This deep contribution is reduced through the incorporation of 40% Cu, which is most likely tied to the improved crystallinity and morphology, suggesting that fewer defects are introduced in the synthesis compared to the reference systems, as confirmed by absorbance log plots (Figure S6). These disorder-related deep levels are also confirmed by the PL emission, as seen in Figure 3c, where the main emission maximum lies at around 1.6 eV as well, with only a small contribution at the band edge (2.3 eV), which agrees well with the band gap obtained from the Elliott fits. This low energy emission is probably caused by self-trapped excitons and defects dominating the emission behavior, which was reported to be induced by exciton–phonon coupling and the resulting ultrafast carrier localization in multiple lead-free perovskite materials. (55−57) Furthermore, the lifetimes are also unaffected by additional Cu doping and occur in the range of only picoseconds (Figure 3d). The detailed spectral trends of PL and lifetime measurements for all samples are shown in Figure S8, with only negligible intensity and lifetime differences evident.

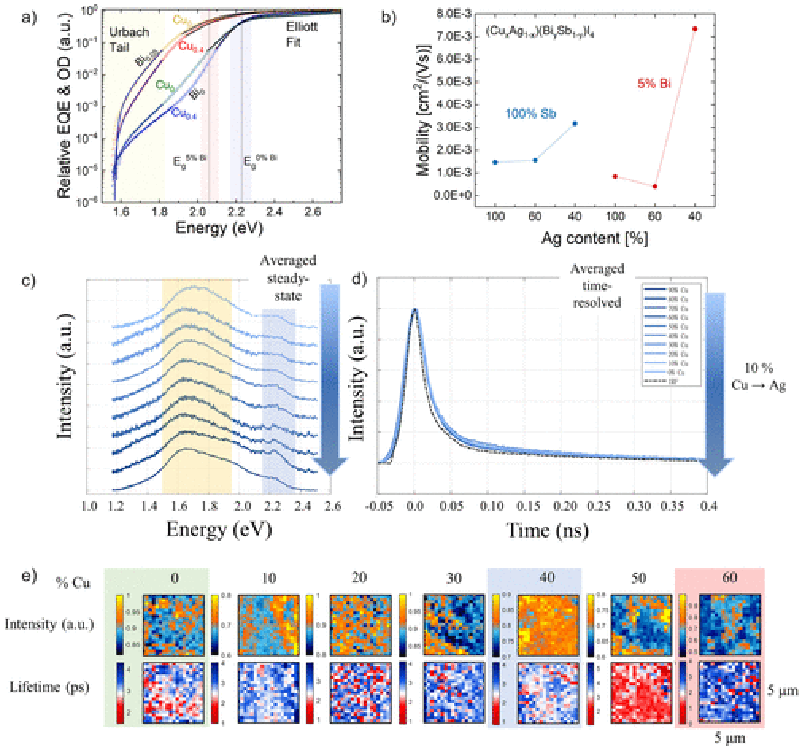

Figure 3. (a) Fitted absorption coefficient of $AgSbI_4$ (green), $Cu_{0.4}Ag_{0.6}SbI_4$ (blue), $AgBi_{0.05}Sb_{0.95}I_4$ (yellow), and $Cu_{0.4}Ag_{0.6}Bi_{0.05}Sb_{0.95}I_4$ (red). Red and blue boxes highlight the band gap extracted from the Elliott fits. The straight lines around the band edge are fitted with Elliott's method and the black lines in the band gap are exponential Urbach tails. (b) Mobility values extracted from time-resolved microwave conductivity measurements for Ag concentrations of 100, 60, and 40% without (blue) and with 5% Bi-substitution (red). (c) Averaged spectra from PL measurements for incremental Cu percentage from 0 to 100% without Bi addition (dark to light blue: increasing Cu content). The yellow box highlights the self-trapped exciton emission and the light blue box highlights the band-to-band emission. (d) Averaged time-resolved PL measurements for incremental Cu percentage from 0 to 100% without Bi addition (dark to light blue: increasing Cu content). (e) Hyperspectral images of the PL intensity and time-resolved PL intensity distribution on a 5 μm × 5 μm large area of a CASI thin film with composition ranging from 0 to 60% Cu/Ag ratio.

Mobility values for the thin films, extracted from time-resolved microwave conductivity (TRMC), highlight an overall increase when the silver content is reduced, as shown in Figure 3b. This is in line with previous reports on the related $Cu_{4x}(AgBi)_{1-x}I_4$ compound, where small polaron formation was found to be responsible for ultrafast charge carrier localization that could be mitigated via the introduction of Cu. (55,56) Note that the extracted charge carrier mobility is a lower estimate, limited by the sensitivity of the setup. Nevertheless, a comparison is feasible, indicating relatively low mobility compared to other lead-free perovskites like $Cs_2AgBiBr_6$ (3–5 cm^2/Vs). (58) Moreover, Bi addition does not increase the overall mobility in the pure $AgSbI_4$, but it significantly boosts the mobility for systems with Cu in excess of 60%.

To connect the optical properties with the morphology changes upon Cu doping, we performed fluorescence-lifetime imaging microscopy (FLIM) measurements; the results are shown in Figure 3e. Here, the intensity of the PL emission and the lifetime are spectrally and spatially resolved on a film area of the size 5 μm × 5 μm. These results confirm the trend of increased homogeneity of the surface of film samples alloyed with 40% Cu, showing the most consistent lifetimes overall and the best (homogeneous) distribution of luminescence intensity. The latter decreases sharply at 50% Cu and above, drastically decreasing the lifetime of the whole sample area. Keeping in mind the similar electronic characteristics over the whole substitution range, these measurements reveal the important role of the A cation in such structures, directing morphology, excitation behavior over a bigger sample size, and, as shown in Figure 5, device performance and statistics.

DFT calculations were then performed to shed light on the impact of composition on the Ag–Sb–I and Cu/Ag–Sb–I rudorffite phases. The ionic positions and cell parameters were optimized on the PBE level of theory, including D3 dispersion corrections, with refined PBE0 + SOC calculations for formation energies and electronic band gaps; see computational details in the Supporting Information. The cubic $ThZr_2H_7$-type $AgSb_2I_7$ stoichiometry, (45,59−61) see Figure S9, is unlikely to form as seen in the large formation energies of 4.86 eV/f.u., see Table 1. Additionally, predicted band gaps of 0.39 eV, far below the experimental values, rule out the existence of $AgSb_2I_7$ stoichiometry, in line with studies on its Bi-based counterpart. (45) $AgSbI_4$ and Ag_3SbI_6 phases show disorder in their positions of Sb and Ag ions; see Figures S10 and S11. Starting from the structure of the Bi-based counterparts, (59,62,63) a configurational screening was performed to obtain low energy configurations using DFT. Both compositions ($AgSbI_4$ and Ag_3SbI_6) show low energy structures with formation energies of −0.01 and 0.03 eV with band gaps of 2.07 and 1.78 eV for $AgSbI_4$ and Ag_3SbI_6, respectively. Recalling the experimental band gap values of ∼ 2.0–2.2 eV, supports the existence of layered $AgSbI_4$ phases, see Figure 4a, while Ag_3SbI_6-rich side phases may contribute to the subgap absorption and emission features. The DOS of the $AgSbI_4$ phase shows the expected dominant role of iodide at the valence band (VB) edge, while the conduction band edge is dominated by Sb and I states from the SbI_6 octahedra, with limited contribution from Ag; see Figure 4b. Note that entropic contributions, neglected in our study, likely contribute to the phase stabilization of such disordered phases.

Table 1. Optimized Lattice Parameters (PBE, D3) of the Low Energy Configurations of the Ag–Sb–I and Cu/Ag–Sb–I Rudorffite Phases[a]

system	formation energy (eV/f.u.)	band gap (eV)	lattice constants (Å)	cell angles (deg)
$AgSb_2I_7$	4.86	0.39	$a = b = c = 14.637$	$\alpha = \beta = \gamma = 90$
$AgSbI_4$	–0.01	2.07	$a = 8.671$	$\alpha = 88.97$
			$b = 8.665$	$\beta = 91.11$
			$c = 20.804$	$\gamma = 120.58$
Ag_3SbI_6	0.03	1.78	$a = 9.178$	$\alpha = 86.57$
			$b = 8.751$	$\beta = 92.47$
			$c = 20.763$	$\gamma = 122.65$
Cu_2AgSbI_6	0.42	1.90	$a = 8.551$	$\alpha = 89.96$
			$b = 8.525$	$\beta = 90.11$
			$c = 21.452$	$\gamma = 119.52$
$Cu_{0.5}Ag_{0.5}SbI_4$	0.14	2.13	$a = 8.671$	$\alpha = 88.97$
			$b = 8.665$	$\beta = 91.11$
			$c = 20.804$	$\gamma = 120.58$

[a] Formation energies per formula unit and electronic band gaps are given at the PBE0 level of theory with the inclusion of SOC corrections on the PBE + D3 optimized geometries. Table S2 summarizes a configurational analysis for each composition.

Moving to the (Cu/Ag)–Sb–I compositions, especially the Cu_2AgSbI_6 phase has recently been proposed to form in the Bi counterparts. (64) The structure of the given phase is highly disordered, with many cations occupying the same lattice positions, requiring a configurational screening; see Figure S12. The proposed low-energy structure shows a formation energy of 0.42 eV/f.u., containing layers of Ag/Cu–I without Sb incorporated; see configuration c11 in Figure S12, which is substantially lower than fully mixed structures; see Table S2. This may point to favorable phase segregation in such compounds. Electronic band gap values of 1.90 eV are in fair agreement with experiments. Still, the successful incorporation of Cu ions over a wide range of Cu/Ag alloying in our experimental investigation raises concerns about the relevance of the Cu_2AgSbI_6 phase. Thus, we performed DFT calculations on the $Cu_{0.5}Ag_{0.5}SbI_4$ composition, keeping the overall A–B–X stoichiometry of 1–1–4 and replacing half of the Ag ions by Cu, as suggested by our XRD data in Figure 1. Interestingly, the formation energy of the $Cu_{0.5}Ag_{0.5}SbI_4$ phase, see Figure 4b, decreases to 0.14 eV/f.u., with a band gap of 2.13 eV, in excellent agreement with our experimental thin films. We further predict an upshift of the VB edge by 0.24 eV compared to the $AgSbI_4$ phase; see Figure 4c. Notably, VB XPS spectra (Figure S2d) show an increase in the VB energy upon Cu addition by ∼0.15–0.25 eV. The energy difference between the VB onset and the

Fermi level (binding energy of 0 eV) decreases from 1.1 eV ($AgSbI_4$) to 0.8 eV (40% Cu) and depends on the Cu content and the presence of Bi. In addition, 0.15 eV binding energy shifts of the core levels such as Cu $2p_{3/2}$, Sb $3d_{5/2}$, or Ag $3d_{5/2}$ (Figure S2a–c) are also observed for these samples, meaning that the Fermi level position inside the band gap is modified by 0.15 eV and that the VB onset is also shifted by 0.15 eV to higher energy. It confirms our DFT results and, most importantly, underlines the existence of the 1:1:4 stoichiometry in our synthesized thin films. Thus, we can expect that the 1:1:4 stoichiometry is accessible over a large range of Cu/Ag alloying. In addition, it can be noted that combining the optical band gap and the energy difference between the VB onset and the Fermi level indicates that the (Cu/Ag)–Sb–I composition materials are rather intrinsic semiconductors.

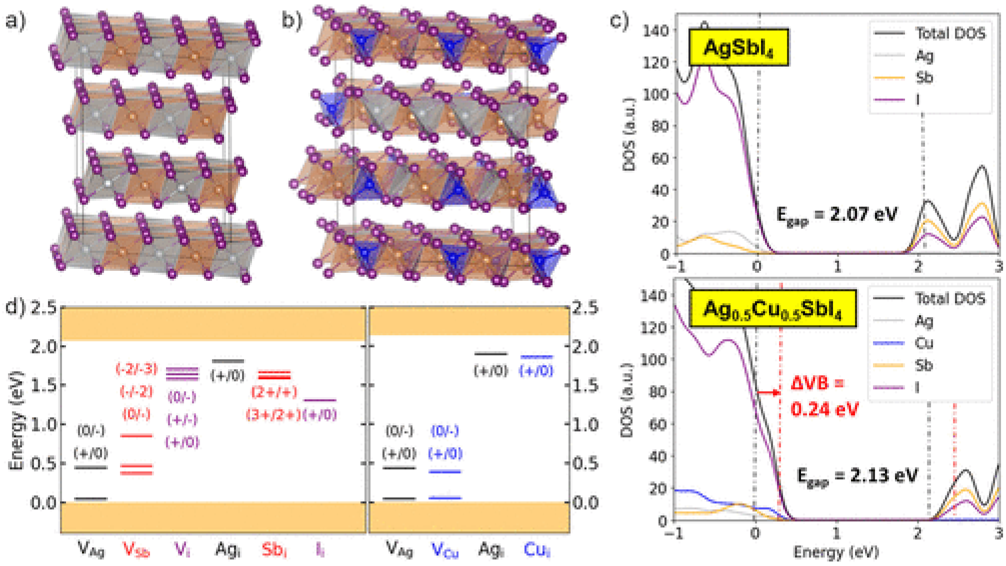

Figure 4. (a,b) Structural representation of $AgSbI_4$ and $Cu_{0.5}Ag_{0.5}SbI_4$, respectively, with the following color codes: Ag = silver, Cu = blue, Sb = orange, and I = purple. (c) Density of states on the PBE0+SOC level of theory of (top) $AgSbI_4$ and (bottom) $Cu_{0.5}Ag_{0.5}SbI_4$. Electronic band gap values are given in each panel. The potential of the considered systems has been aligned with respect to the vacuum level to obtain the VB shift between $AgSbI_4$ and $Cu_{0.5}Ag_{0.5}SbI_4$, as highlighted in red. The VB maximum of the $AgSbI_4$ phase has been set to zero energy. (d) Thermodynamic ionization levels (TILs) of point defects, vacancies V_X, and interstitials X_i for each element X = (Ag, Cu, Sb, and I), based on hybrid PBE0 + D3 DFT calculations with inclusion of SOC. Orange parts highlight the VB band (bottom) and conduction band (top). Right box: comparison of Ag and Cu TILs. Computational details on the defect calculations are provided in the Supporting Information.

We further calculate the defect formation energies (DFEs), see Figures S14 and S15, and thermodynamic ionization levels (TILs), see Figure 4d, for the pure $AgSbI_4$ and the alloyed $Cu_{0.5}Ag_{0.5}SbI_4$ compounds. All geometries were optimized on the PBE + D3 level of theory with refined calculations for DFE and TILs based on the PBE0 level of theory with the inclusion of spin–orbit coupling corrections. We observe low DFEs of 0.16 eV for Ag vacancies (V_{Ag}^-) and interstitials (Ag_i^+), representing hole and electron trap states at 0.44 eV above the VBM and 0.25 eV below the CBM; see Figures 4d and S14. This suggests that subgap emission features at 1.6 eV (i.e., 0.6 eV below the band gap measured in Figure 3a) may likely be caused by the recombination of electrons trapped at Ag vacancies. The low formation energies of Ag point defects further are in line with features of Ag–Bi–I compounds that previously have been considered for ionic conduction due to their mobile Ag ions. (62) Notably, Sb and I point defects also act as trap states within the band gap; see Figure 4d, while showing moderate formation energies of ~0.7 to 0.9 eV, thus being of less relevance for the optoelectronic properties of $AgSbI_4$. Moving toward the alloyed $Cu_{0.5}Ag_{0.5}SbI_4$, we observe negligible differences in the TILs and DFEs (Figure S15) for Ag and Cu vacancies and interstitials, in line with the low dependence of subgap emission on Cu/Ag alloying, as shown in Figure 4c. This suggests further that the reduction of subgap absorption upon Cu addition is due to the growth of more homogeneous morphologies (see Figure 2) rather than a suppression of point defect formation. Consequently, Cu alloying is mainly relevant for reducing AgI-rich side phases, while the concentration of incremental Cu alloying shifts the type of detrimental defects between Ag and Cu.

After the structural and electronic properties of the CASI rudorffites were elaborated, photovoltaic devices were fabricated in the n-i-p architecture with increasing amounts of Cu. Mesoporous TiO_2 was used as the electron transport layer and PTAA as the hole transport layer. (28,29,65) The statistical analysis of the device performance can be seen in Figure 5a–f. First, the overall performance increases significantly when employing only a small substitution of 5% Bi, attributed to the band gap decrease. Second, Cu addition also increases the overall performance until an optimal concentration of 40%, while the performance breaks down at a higher level. Interestingly, the minor incorporation of Bi additionally stabilizes the performance over a wider range of Cu/Ag ratios, almost up to 80%. We attribute this impact of Bi to the improved homogeneity of the morphology as seen in Figure 2f, hinting at a highly beneficial role of BiI_3 in the precursor solution. In the Bi-free series, samples prepared with 40% Cu are generally the most efficient, showing the overall highest PCE, mostly due to the increased current density. Notably, the low open circuit voltage is the main bottleneck in these systems, as also suggested previously. (29,30) In our studies, only samples with added Bi surpass the 0.4 V open circuit voltage in some cases, whereas Cu-alloyed samples show only small improvements. We attribute the low voltage to nonradiative recombination processes mediated by Ag point defects, representing trap states with low formation energies as shown by our DFT calculations, and ultrafast carrier localization. (53,55)

To further estimate the potential of Sb-based rudorffites for indoor photovoltaics, EQE measurements were carried out on well-performing solar cells with and without white light background illumination. As shown in Figure 5g, the EQE measured under white light illumination at 100 mW/cm^2 is comparably small, with a maximum of 20% for Cu-alloyed films at 450 nm without Bi and at 550 nm with Bi. Interestingly, when using a chopped white light source without a white light bias, the overall EQE increases significantly by approximately 10% for all thin films, except $Cu_{0.4}Ag_{0.6}SbI_4$. This could be explained by a different recombination mechanism at high fluence intensities in this system, as seen in the TRMC curves in Figure S7b. The EQE increase is in line with the behavior of Cu_2AgBiI_6 rudorffites, where the efficiency for indoor light illumination almost doubles up to 10% iPCE, (34) being attributed to reduced nongeminate recombination, which seems to be an intrinsic feature of (Cu/Ag)–(Sb/Bi)–I-based materials.

Although the initial performance falls behind Bi-based “rudorffites”, (28,34,60) this class of materials offers great potential for indoor applications while being easily tunable. Furthermore, our results demonstrate the compositional freedom of solution-processed rudorffites. We propose that through stoichiometry tweaking and precursor engineering–i.e., by employing acetates or other metal sources (15,22)–or further additive modification, the performance could be strongly improved to offer a viable alternative for low-cost indoor photovoltaics.

Conclusions

To summarize, we successfully synthesized “rudorffite”-type Cu/Ag–Sb–I thin films using the Lewis-base additive thiourea. We establish control of the thin film morphology by partial alloying of Ag with Cu atoms, resulting in homogeneous coverage, which was even improved upon partial substitution with Bi. DFT calculations and optical characterization point to the formation of a $AgSbI_4$ phase in the pure Ag case and the incorporation of Cu ions, partially replacing Ag and forming $Cu_{1-x}Ag_xSbI_4$. Other phases that have been previously discussed for the Bi-based counterparts could be ruled out due to larger formation energies or lower predicted band gaps. Our results further reveal the detrimental role of Ag point defects, which induce sub-band gap electronic states that may act as recombination centers, resulting in subgap emission and absorption features. We further demonstrate that Cu alloying does not significantly alter the electronic band gap, which consequently represents a facile strategy for the optimization of Sb-based rudorffites. Solar cells based on Sb-based rudorffites show low power conversion efficiencies of around 0.3%, mainly limited by large losses in the V_{OC}. Substituting the optimal ratio of Cu/Ag with a small amount of 5% bismuth to $\mathrm{Cu}_{0.4}\mathrm{Ag}_{0.6}\mathrm{Sb}_{0.95}\mathrm{Bi}_{0.05}\mathrm{I}_4$ raises the efficiencies to up to 0.7%, mainly through a reduction of the electronic band gap and an increased J_{SC}. We observe an apparent stabilization of current density and open-circuit voltage upon addition of Bi over a wide range of Cu/Ag alloys. Finally, white light bias-free EQE measurements suggest a much-improved performance of these materials for indoor photovoltaic applications, which we attribute to reduced geminate recombination at low light intensity. These observations offer opportunities for the control and design of novel Sb-based rudorffites as perovskite-inspired semiconductors with the potential for diverse optoelectronic applications such as indoor photovoltaics.

Experimental/Methods

Precursor Solution

To synthesize (Cu/Ag)–(Bi/Sb)–I films, the corresponding iodides were dissolved in a 1:1 vol % mixture of DMF/DMSO in a 0.6 M precursor solution with a 1 wt % additive of TU.

1 mL of precursor solutions for the CASI systems were weighed in as follows: x is the molar ratio ($\mathrm{Cu}_x\mathrm{Ag}_{1-x}\mathrm{SbI}$); the masses are given in weight/amount of substance [mg/mmol] (Table 2).

Table 2. Precursors and Respective Weights/Substance Amounts for the Thin Film Synthesis of CASI Thin Films

***x* (molar ratio)**	**0**	**0.1**	**0.2**	**0.3**	**0.4**	**0.5**	**0.6**	**0.7**	**0.8**	**0.9**	**1**
AgI (Sigma-Aldrich)	140.8/0.6	126.8/0.54	112.7/0.48	98.6/0.42	84.5/0.36	70.4/0.3	56.3/0.24	42.3/0.18	28.2/0.12	14.1/0.06	0/0
CuI (Sigma-Aldrich)	0/0	11.4/0.06	22.9/0.12	34.3/0.18	45.7/0.24	57.1/0.3	68.6/0.36	80.0/0.42	91.4/0.48	102.8/0.54	114.27/0.6
SbI_3(Alfa Aesar)	301.4/0.6	301.4/0.6	301.4/0.6	301.4/0.6	301.4/0.6	301.4/0.6	301.4/0.6	301.4/0.6	301.4/0.6	301.4/0.6	301.4/0.6

To these mixtures, 1 wt % with respect to the total precursor weight of TU was added (4.42 mg, 0.06 mmol, Sigma-Aldrich) and dissolved in 0.5 mL DMF and 0.5 mL DMSO. Furthermore, for 5% Bi-substitution, 17.69 mg (0.03 mmol) BiI_3 was added, and only 286.4 mg (0.57 mmol) SbI_3 was used.

Thin Film Deposition

All solutions were heated at 70 °C on a hot plate in a nitrogen atmosphere for 30 min prior to spin-coating. For thin film deposition, 70 μL of the precursor solution was spin-coated on different substrates at 3000 rpm for 10 s, followed by 6000 rpm for 50 s. Varying substrate types were cleaned with oxygen plasma under vacuum (up to 10^{-4} mbar). Glass and fluorine-doped tin oxide (FTO) substrates were cleaned at 50% power for 5 min with a Diener Femto Plasma Etcher.

X-ray Analysis

XRD data of thin films were recorded on a Bruker D8 Discover instrument operating at 40 kV and 30 mA with Cu Kα radiation (λ = 1.5406 Å) and a position-sensitive LynxEye detector. XRD patterns were measured in the range of 2θ = 5–60° with a step size of 0.05°. Powders were measured on a STOE STADI P diffractometer with Cu Kα radiation (λ = 1.5406 Å) and a Ge(111) single-crystal monochromator equipped with a DECTRIS solid-state strip detector MYTHEN 1K, which was used for wide-angle X-ray diffraction measurements in transmission mode. Powder patterns were measured in the range of 2θ = 5–60° with a resolution of 0.05° and a step size between 0.5 and 4° with a counting time of 20–90 s per step.

Device Fabrication

A sol–gel approach was used to deposit the compact TiO_2 layer from a solution containing 0.23 M titanium isopropoxide (Sigma-Aldrich, 99.999%) and 0.013 M HCl in isopropanol (IPA). The solution of 250 μL per 6 × 6 cm^2 substrate size was spin-coated dynamically on top of the substrate at 2000 rpm for 45 s, dried at 150 °C for 10 min, and annealed at 500 °C for 45 min.

In devices with a mesoporous TiO_2 layer, an approximately 150 nm thick, mesoporous (mp)-TiO_2 layer was applied by spin-coating 100 μL of a TiO_2 nanoparticle paste (Dyesol DSL 18NR-T) diluted in absolute ethanol (1:6 weight ratio) onto the above compact TiO_2 layer at 2500 rpm for 30 s, followed by subsequent annealing at 500 °C for 45 min under ambient conditions.

PTAA (12 mg, average molecular weight Mn = 30,000) was dissolved in 1 mL of toluene, and the resulting solution was filtered using a syringe filter (pore diameter 0.45 μm). A 70 μL aliquot of the filtered solution was spin-coated on top of the active layer in a single-step spin coating program at 3000 rpm for 35 s, and the obtained films were annealed at 100 °C for 5 min.

The top electrode with a thickness of 40 nm was deposited by thermally evaporating gold under a vacuum (at $\sim 10^{-7}$ mbar).

SEM Measurements

For analysis of the thin film morphology, thickness, and composition, scanning electron microscopy (SEM) was performed on an FEI Helios Nanolab G3 UC-DualBeam SEM with an acceleration voltage between 2 and 5 keV.

X-ray Photoelectron Spectroscopy

The samples were sealed in a nitrogen atmosphere and delivered to Darmstadt, where they were opened in a glovebox filled with N_2, and then transferred under vacuum to the DAISY-SOL lab's cluster tool. XPS was then performed with a Thermo Fisher VG Escalab 250 spectrometer in an analytic chamber with a pressure kept below 3×10^{-9} mbar. A monochromatic Al Kα X-ray source ($h\nu$ = 1486.6 eV) operating at 12.5 mA and 14.2 kV was used for the XPS experiment without a charge neutralizer. The measurement mode was adjusted to get a lateral resolution of 650 μm in diameter and overcome possible inhomogeneity at the sample surface.

The high-resolution spectra were acquired with a pass energy of 10 eV, a step size of 0.05 eV, and a dwell time of 50 ms; up to 60 scans were made to increase the signal-to-noise ratio.

XPS spectra were calibrated using the Fermi level of silver (0 eV) as well as the binding energy of the Au $4f_{7/2}$ emission line (84.0 eV), the Ag $3d_{5/2}$ emission line (368.26 eV–fwhm at a pass energy of 10 eV equal to 0.53 eV), and the Cu $2p_{3/2}$ emission line (932.67 eV). The Fermi level value was determined with a sigmoid fit and taking the position where the intensity is at 50%. Before the measurement, all calibration samples were cleaned by using Ar sputtering (3 kV, for 180 s). The instrumental resolution was measured using the Fermi level of the cleaned silver, which was 0.44 eV for XPS (pass energy of 10 eV).

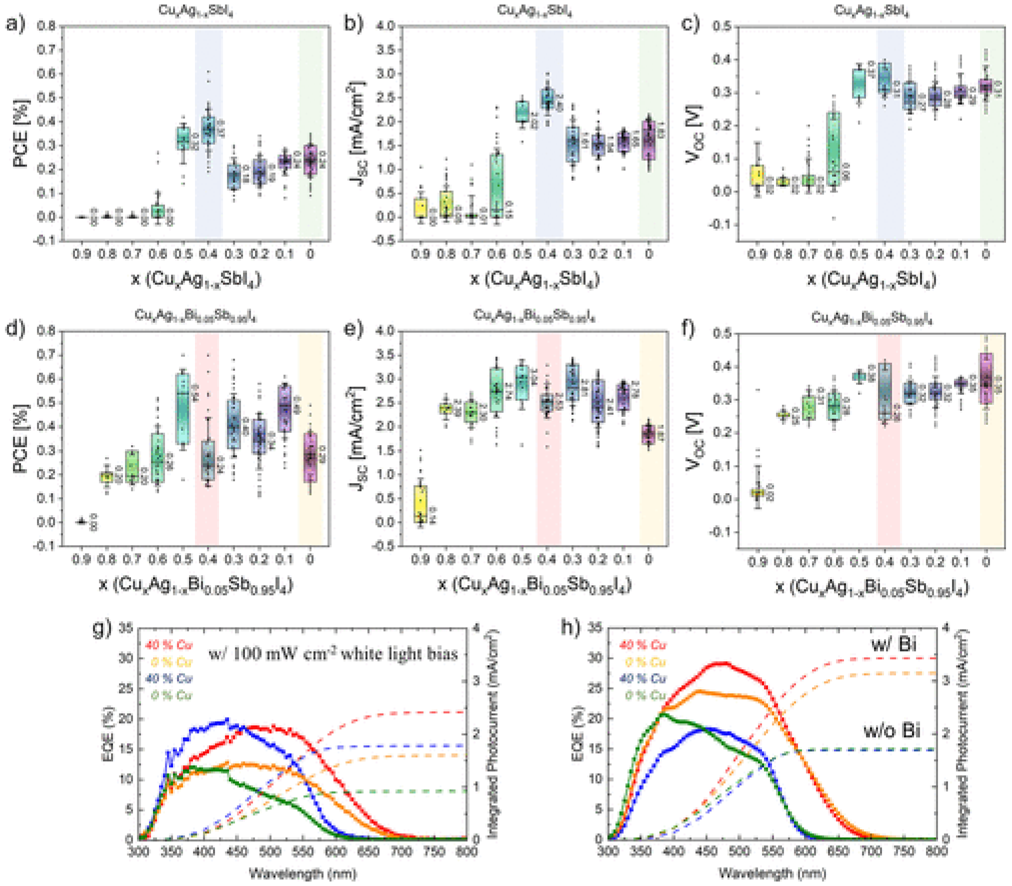

Figure 5. Characterization of the photovoltaic devices. (a–c) PCE, J_{sc}, and V_{oc} statistical box plots with median, interquartile range, and statistical outliers for 10% changes of the Cu/Ag ratio from $Cu_{0.9}Ag_{0.1}SbI_4$ to $Cu_{0.0}Ag_{1.0}SbI_4$. The same color scheme for the colored boxes as for Figure 4a was used to highlight the reference and the most efficient alloying step. (d–f) PCE, J_{sc}, and V_{oc} statistical box plots with median, interquartile range, and statistical outliers for 10% changes of Cu/Ag ratio with fixed 5% Bi content from $Cu_{0.9}Ag_{0.1}Bi_{0.05}Sb_{0.95}I_4$ to $Cu_{0.0}Ag_{1.0}$ $Bi_{0.05}Sb_{0.95}I_4$. The same color scheme for the colored boxes as for Figure 4a was used to highlight the reference and the most efficient alloying step. (g,h) EQE spectra and integrated photocurrent density of the most efficient solar cells for $AgSbI_4$ (green), $Cu_{0.4}Ag_{0.6}SbI_4$ (blue), $AgBi_{0.05}Sb_{0.95}I_4$ (orange), and $Cu_{0.4}Ag_{0.6}Bi_{0.05}Sb_{0.95}I_4$ (red). The data in (g) were measured with a constant 100 mW/cm^2 white light source in the background, while the data in (h) were measured without white light bias.

UV–Vis Spectroscopy

UV–vis spectroscopy was conducted with a PerkinElmer Lambda 1050 instrument equipped with a 150 mm integrating sphere. A tungsten–halogen and a deuterium lamp were used to create visible and ultraviolet light. The measurement interval was chosen from 350 to 900 nm with a monochromator step size of 2 nm.

PL Measurements

For PL measurements, hyperspectral images, and time-resolved PL images, a home-built confocal laser scanning microscope was used. It is based on a microscope body (NIKON) that is combined with an *xyz*-piezo-scanning stage (PHYSIK INSTRUMENTE). The samples were measured upside down in the epi-direction with an air objective (1.4 NA, Apo-Chromat, NIKON). A beamsplitter (MELLES GRIOT 03BTL005) and a spectral 490 nm long-pass filter were used to separate the laser from the PL light. A sub-picosecond laser (iChrome TOPTICA), which is tunable from 476 to 645 nm, was used for excitation. Here, we measured only with the 476 nm laser light, which was additionally filtered by a band-pass of 473/10 nm (CHROMA) in the excitation arm. The detection side consists of two parts that are separated by a flippable mirror. One has an avalanche photo diode (APD, type: MPD PDM, detector size 50 × 50 μm), which can be combined with time-correlated single-photon counting (TCSPC) electronics (BECKER UND HICKEL) to measure time-resolved PL-transients. The second part consists of a spectrometer (ANDOR SHAMROCK SRi303) combined with an open electrode CCD camera (ANDOR NEWTON DU920) for recording spectra. The data were recorded using a customized LABVIEW (National Instruments) program that combines the manufacturers' software with our desired measurements. Further processing and analysis were carried out using MATLAB (MATHWORKS) programs to obtain the PL spectra, TCSPC transients, and the images.

TRMC Measurements

Thin films on sapphire substrates were placed in a microwave cavity. The TRMC technique was used to measure the change in reflected microwave (9 GHz) power after pulsed excitation (repetition rate 1 kHz) of the samples at 355 nm using the third harmonic of a Nd/YAG laser. The layers were illuminated from the glass side. (58)

Solar Cell Characterization

Photovoltaic device performance was measured with a Keithley 2400 source meter in air at 25 °C under illumination by a Newport Oriel Sol2A solar simulator, which was calibrated to 100 mW/cm^2 with a Fraunhofer ISE-certified silicon cell with a mismatch factor of 1.01. The active area of the solar cell was defined with a square metal aperture mask of 0.0831 cm^2.

EQE Measurements

Measurements were performed on a home-built setup with a halogen lamp, a monochromator, and a silicon reference diode. The light was chopped at 330 Hz, and the signal was detected through a lock-in amplifier. The setup was calibrated with a silicon solar cell, and no bias light was applied.

Computational Details

DFT calculations were performed on Ag–Sb–I and alloyed Cu/Ag–Sb–I rudorffites. Cell parameters were refined within the Quantum ESPRESSO software package (66) (vc-relax) using the GGA-PBE exchange correlation functional. (67) Electron-ion interactions were described by scalar relativistic ultrasoft pseudopotentials (Ag, 11 electrons, 5s^2, 4p^9; Cu, 11 electrons, 4s^2, 3d^9; Sb, 5 electrons, 5s^2, 5p^3; and I, 7 electrons, 5s^2, 5p^5). Plane-wave basis set cutoffs for the smooth part of the wave functions and the augmented density were 40 and 320 Ry, respectively. The Brillouin zone was sampled using a 4 × 4 × 1 Monkhorst–Pack grid. (68) Dispersion corrections were accounted for by the DFT-D3 scheme. (69)

Accurate electronic band gaps were calculated using the PBE0 functional, (70) including spin–orbit coupling within the Quantum ESPRESSO package. (66) Here, we used full relativistic norm-conserving pseudopotentials (Ag, 19 electrons, $4s^2$, $4p^6$, $4d^{10}$, $5s^2$, $4p^9$; Sb, 15 electrons, $4d^{10}$, $5s^2$, $5p^3$; and I, 7 electrons, $5s^2$, $5p^5$) with a cutoff on the wave functions of 40 and 80 Ry on the Fock grid and sampling the Brillouin zone using a 2 × 2 × 1 Monkhorst–Pack grid. PDOS plots were generated with a Gaussian smearing of 0.1 eV.

Supporting Information

The Supporting Information is available free of charge at https://pubs.acs.org/doi/10.1021/acs.chemmater.3c01837.

- Experimental procedures, additional experimental data (XPS, XRD, UV–vis, JV, and PL), computational method (DFT), compositional analysis, and further computational results (PDF)

Terms & Conditions

Author Information

- Corresponding Author

Thomas Bein - *Department of Chemistry and Center for NanoScience (CeNS), University of Munich (LMU), Butenandtstr. 11, 81377 Munich, Germany*; https://orcid.org/0000-0001-7248-5906; Email: bein@lmu.de

- Authors

Rik Hooijer - *Department of Chemistry and Center for NanoScience (CeNS), University of Munich (LMU), Butenandtstr. 11, 81377 Munich, Germany*; https://orcid.org/0000-0002-0038-2649

Andreas Weis - *Department of Chemistry and Center for NanoScience (CeNS), University of Munich (LMU), Butenandtstr. 11, 81377 Munich, Germany*; https://orcid.org/0000-0003-0128-4116

Waldemar Kaiser - *Computational Laboratory for Hybrid/Organic Photovoltaics (CLHYO), Istituto CNR di Scienze e Tecnologie Chimiche “Giulio Natta” (CNR-SCITEC), 06123 Perugia, Italy*; https://orcid.org/0000-0001-9069-690X

Alexander Biewald - *Department of Chemistry and Center for NanoScience (CeNS), University of Munich (LMU), Butenandtstr. 11, 81377 Munich, Germany*

Patrick Dörflinger - *Experimental Physics VI, Julius Maximilian University of Würzburg, 97074 Würzburg, Germany*

Clément Maheu - *Surface Science Laboratory, Department of Materials and Earth Sciences, Technical University of Darmstadt, Otto-Berndt-Strasse 3, 64287 Darmstadt, Germany*

Oleksandr Arsatiants - *Department of Chemistry and Center for NanoScience (CeNS), University of Munich (LMU), Butenandtstr. 11, 81377 Munich, Germany*

David Helminger - *Department of Chemistry and Center for NanoScience (CeNS), University of Munich (LMU), Butenandtstr. 11, 81377 Munich, Germany*

Vladimir Dyakonov - *Experimental Physics VI, Julius Maximilian University of Würzburg, 97074 Würzburg, Germany*; https://orcid.org/0000-0001-8725-9573

Achim Hartschuh - *Department of Chemistry and Center for NanoScience (CeNS), University of Munich (LMU), Butenandtstr. 11, 81377 Munich, Germany*

Edoardo Mosconi - *Computational Laboratory for Hybrid/Organic Photovoltaics (CLHYO), Istituto CNR di Scienze e Tecnologie Chimiche "Giulio Natta" (CNR-SCITEC), 06123 Perugia, Italy*

Filippo De Angelis - *Computational Laboratory for Hybrid/Organic Photovoltaics (CLHYO), Istituto CNR di Scienze e Tecnologie Chimiche "Giulio Natta" (CNR-SCITEC), 06123 Perugia, Italy*; *Department of Chemistry, Biology and Biotechnology, University of Perugia and INSTM, Perugia 06123, Italy*; *Department of Natural Sciences & Mathematics, College of Sciences & Human Studies, Prince Mohammad Bin Fahd University, Al Khobar 31952, Saudi Arabia*; *SKKU Institute of Energy Science and Technology (SIEST) Sungkyunkwan University, Suwon 440-746, Korea*; https://orcid.org/0000-0003-3833-1975

- Author Contributions

R.H. and A.W. contributed equally to this work.

- Notes

The authors declare no competing financial interest.

Acknowledgments

The authors acknowledge funding from the Bavarian Network "Solar Technologies Go Hybrid", the German Science Foundation (DFG) focus program SPP 2196 (projects BE 1042/10-1, 424101351, 506623857, 423746744 and 424707803), and the DFG Excellence Cluster e-conversion (EXC 2089/1-390776260). The authors thank Dr. Steffen Schmidt for performing the SEM measurements. W.K., E.M., and F.D.A. acknowledge funding from the European Union's Horizon Europe research and innovation programme under grant agreement no. 101082176–VALHALLA and from the European Union-NextGenerationEU under the Italian Ministry of University and Research (MUR) National Innovation Ecosystem grant ECS00000041–VITALITY. The views and opinions expressed are, however, those of the author(s) only and do not necessarily reflect those of the European Union or CINEA. Neither the European Union nor the granting authority can be held responsible for them. F.D.A. acknowledges Università degli Studi di Perugia and MUR for support within the project Vitality.

References

This article references 70 other publications.

1. Divitini, G.; Cacovich, S.; Matteocci, F.; Cinà, L.; Di Carlo, A.; Ducati, C. In situ observation of heat-induced degradation of perovskite solar cells. *Nat. Energy* **2016**, *1* (2), 15012, DOI: 10.1038/nenergy.2015.12
2. Boyd, C. C.; Cheacharoen, R.; Leijtens, T.; McGehee, M. D. Understanding Degradation Mechanisms and Improving Stability of Perovskite Photovoltaics. *Chem. Rev.* **2019**, *119* (5), 3418– 3451, DOI: 10.1021/acs.chemrev.8b00336
3. Dunfield, S. P.; Bliss, L.; Zhang, F.; Luther, J. M.; Zhu, K.; van Hest, M. F. A. M.; Reese, M. O.; Berry, J. J. From Defects to Degradation: A Mechanistic Understanding of Degradation in Perovskite Solar Cell Devices and Modules. *Adv. Energy Mater.* **2020**, *10* (26), 1904054, DOI: 10.1002/aenm.201904054
4. Schmidt-Mende, L.; Dyakonov, V.; Olthof, S.; Ünlü, F.; Lê, K. M. T.; Mathur, S.; Karabanov, A. D.; Lupascu, D. C.; Herz, L. M.; Hinderhofer, A.; Schreiber, F.; Chernikov, A.; Egger, D. A.; Shargaieva, O.; Cocchi, C.; Unger, E.; Saliba, M.; Byranvand, M. M.; Kroll, M.; Nehm, F.; Leo, K.; Redinger, A.; Höcker, J.; Kirchartz, T.; Warby, J.; Gutierrez-Partida, E.; Neher, D.; Stolterfoht, M.; Würfel, U.; Unmüssig, M.; Herterich, J.; Baretzky, C.; Mohanraj, J.; Thelakkat, M.; Maheu, C.; Jaegermann, W.; Mayer, T.; Rieger, J.; Fauster, T.; Niesner, D.; Yang, F.; Albrecht, S.; Riedl, T.; Fakharuddin, A.; Vasilopoulou, M.; Vaynzof, Y.; Moia, D.; Maier, J.; Franckevičius, M.; Gulbinas, V.; Kerner, R. A.; Zhao, L.; Rand, B. P.; Glück, N.; Bein, T.; Matteocci, F.; Castriotta, L. A.; Di Carlo, A.; Scheffler, M.; Draxl, C. Roadmap on organic-inorganic hybrid perovskite semiconductors and devices. *APL Mater.* **2021**, *9* (10), 109202, DOI: 10.1063/5.0047616
5. Grätzel, M. The Rise of Highly Efficient and Stable Perovskite Solar Cells. *Acc. Chem. Res.* **2017**, *50* (3), 487– 491, DOI: 10.1021/acs.accounts.6b00492
6. Krebs, F. C.; Espinosa, N.; Hösel, M.; Søndergaard, R. R.; Jørgensen, M. 25th anniversary article: Rise to power-OPV-based solar parks. *Adv. Mater.* **2014**, *26* (1), 29– 39, DOI: 10.1002/adma.201302031
7. Li, H.; Zhang, W. Perovskite Tandem Solar Cells: From Fundamentals to Commercial Deployment. *Chem. Rev.* **2020**, *120* (18), 9835– 9950, DOI: 10.1021/acs.chemrev.9b00780
8. Kim, G.-W.; Petrozza, A. Defect Tolerance and Intolerance in Metal-Halide Perovskites. *Adv. Energy Mater.* **2020**, *10* (37), 2001959, DOI: 10.1002/aenm.202001959
9. Steirer, K. X.; Schulz, P.; Teeter, G.; Stevanovic, V.; Yang, M.; Zhu, K.; Berry, J. J. Defect Tolerance in Methylammonium Lead Triiodide Perovskite. *ACS Energy Lett.* **2016**, *1* (2), 360– 366, DOI: 10.1021/acsenergylett.6b00196
10. Ganose, A. M.; Savory, C. N.; Scanlon, D. O. Beyond methylammonium lead iodide: prospects for the emergent field of ns2 containing solar absorbers. *Chem. Commun.* **2017**, *53* (1), 20– 44, DOI: 10.1039/C6CC06475B
11. Kurchin, R. C.; Gorai, P.; Buonassisi, T.; Stevanović, V. Structural and Chemical Features Giving Rise to Defect Tolerance of Binary Semiconductors. *Chem. Mater.* **2018**, *30* (16), 5583– 5592, DOI: 10.1021/acs.chemmater.8b01505
12. Brandt, R. E.; Poindexter, J. R.; Gorai, P.; Kurchin, R. C.; Hoye, R. L. Z.; Nienhaus, L.; Wilson, M. W. B.; Polizzotti, J. A.; Sereika, R.; Žaltauskas, R.; Lee, L. C.; MacManus-Driscoll, J. L.; Bawendi, M.; Stevanović, V.; Buonassisi, T. Searching for "Defect-Tolerant" Photovoltaic Materials: Combined Theoretical and Experimental Screening. *Chem. Mater.* **2017**, *29* (11), 4667– 4674, DOI: 10.1021/acs.chemmater.6b05496

13. Nasti, G.; Abate, A. Tin Halide Perovskite (ASnX 3) Solar Cells: A Comprehensive Guide toward the Highest Power Conversion Efficiency. *Adv. Energy Mater.* **2020**, *10* (13), 1902467, DOI: 10.1002/aenm.201902467
14. Serrano-Lujan, L.; Espinosa, N.; Larsen-Olsen, T. T.; Abad, J.; Urbina, A.; Krebs, F. C. Tin- and Lead-Based Perovskite Solar Cells under Scrutiny: An Environmental Perspective. *Adv. Energy Mater.* **2015**, *5* (20), 1501119, DOI: 10.1002/aenm.201501119
15. Weis, A.; Ganswindt, P.; Kaiser, W.; Illner, H.; Maheu, C.; Glück, N.; Dörflinger, P.; Armer, M.; Dyakonov, V.; Hofmann, J. P.Heterovalent Tin Alloying in Layered MA3Sb2I9 Thin Films: Assessing the Origin of Enhanced Absorption and Self-Stabilizing Charge States. *J. Phys. Chem. C* **2022**, *126* (49), 21040– 21049, DOI: 10.1021/acs.jpcc.2c06106
16. Leijtens, T.; Prasanna, R.; Gold-Parker, A.; Toney, M. F.; McGehee, M. D. Mechanism of Tin Oxidation and Stabilization by Lead Substitution in Tin Halide Perovskites. *ACS Energy Lett.* **2017**, *2* (9), 2159– 2165, DOI: 10.1021/acsenergylett.7b00636
17. Ricciarelli, D.; Meggiolaro, D.; Ambrosio, F.; De Angelis, F. Instability of Tin Iodide Perovskites: Bulk p-Doping versus Surface Tin Oxidation. *ACS Energy Lett.* **2020**, *5* (9), 2787– 2795, DOI: 10.1021/acsenergylett.0c01174
18. Aldamasy, M.; Iqbal, Z.; Li, G.; Pascual, J.; Alharthi, F.; Abate, A.; Li, M. Challenges in tin perovskite solar cells. *Phys. Chem. Chem. Phys.* **2021**, *23* (41), 23413– 23427, DOI: 10.1039/D1CP02596A
19. Tress, W.; Sirtl, M. T. Cs 2 AgBiBr 6 Double Perovskites as Lead-Free Alternatives for Perovskite Solar Cells?. *Sol. RRL* **2022**, *6* (2), 2100770, DOI: 10.1002/solr.202100770
20. Hoye, R. L. Z.; Eyre, L.; Wei, F.; Brivio, F.; Sadhanala, A.; Sun, S.; Li, W.; Zhang, K. H. L.; MacManus-Driscoll, J. L.; Bristowe, P. D.; Friend, R. H.; Cheetham, A. K.; Deschler, F. Fundamental Carrier Lifetime Exceeding 1 µs in Cs 2 AgBiBr 6 Double Perovskite. *Adv. Mater. Interfaces* **2018**, *5* (15), 1800464, DOI: 10.1002/admi.201800464
21. Sirtl, M. T.; Hooijer, R.; Armer, M.; Ebadi, F. G.; Mohammadi, M.; Maheu, C.; Weis, A.; van Gorkom, B. T.; Häringer, S.; Janssen, R. A. J.2D/3D Hybrid Cs2AgBiBr6 Double Perovskite Solar Cells: Improved Energy Level Alignment for Higher Contact-Selectivity and Large Open Circuit Voltage. *Adv. Energy Mater.* **2022**, *12* (7), 2103215, DOI: 10.1002/aenm.202103215
22. Giesbrecht, N.; Weis, A.; Bein, T. Formation of stable 2D methylammonium antimony iodide phase for lead-free perovskite-like solar cells. *J. Phys.: Energy* **2020**, *2* (2), 024007, DOI: 10.1088/2515-7655/ab78ef
23. McCall, K. M.; Stoumpos, C. C.; Kostina, S. S.; Kanatzidis, M. G.; Wessels, B. W. Strong Electron-Phonon Coupling and Self-Trapped Excitons in the Defect Halide Perovskites A 3 M 2 I 9 (A = Cs, Rb; M = Bi, Sb). *Chem. Mater.* **2017**, *29* (9), 4129– 4145, DOI: 10.1021/acs.chemmater.7b01184
24. McCall, K. M.; Stoumpos, C. C.; Kontsevoi, O. Y.; Alexander, G. C. B.; Wessels, B. W.; Kanatzidis, M. G. From 0D Cs 3 Bi 2 I 9 to 2D Cs 3 Bi 2 I 6 Cl 3: Dimensional Expansion Induces a Direct Band Gap but Enhances Electron-Phonon Coupling. *Chem. Mater.* **2019**, *31* (7), 2644– 2650, DOI: 10.1021/acs.chemmater.9b00636
25. Giovilli, G.; Albini, B.; Grisci, V.; Bonomi, S.; Moroni, M.; Mosconi, E.; Kaiser, W.; De Angelis, F.; Galinetto, P.; Malavasi, L. Band gap tuning through cation and halide alloying in mechanochemically synthesized Cs 3 (Sb 1- x Bi x) 2 Br 9 and Cs 3 Sb 2 (I 1- x Br x) 9 solid solutions. *J. Mater. Chem. C* **2023**, *11*, 10282– 10291, DOI: 10.1039/D3TC01492D
26. Harikesh, P. C.; Mulmudi, H. K.; Ghosh, B.; Goh, T. W.; Teng, Y. T.; Thirumal, K.; Lockrey, M.; Weber, K.; Koh, T. M.; Li, S.; Mhaisalkar, S.; Mathews, N. Rb as an Alternative Cation for Templating Inorganic Lead-Free Perovskites for Solution Processed Photovoltaics. *Chem. Mater.* **2016**, *28* (20), 7496– 7504, DOI: 10.1021/acs.chemmater.6b03310
27. Mitzi, D. B. Templating and structural engineering in organic-inorganic perovskites. *J. Chem. Soc., Dalton Trans.* **2001**, *0* (1), 1– 12, DOI: 10.1039/b007070j

28. Turkevych, I.; Kazaoui, S.; Ito, E.; Urano, T.; Yamada, K.; Tomiyasu, H.; Yamagishi, H.; Kondo, M.; Aramaki, S. Photovoltaic Rudorffites: Lead-Free Silver Bismuth Halides Alternative to Hybrid Lead Halide Perovskites. *ChemSusChem* **2017**, *10* (19), 3754– 3759, DOI: 10.1002/cssc.201700980
29. Lu, C.; Zhang, J.; Sun, H.; Hou, D.; Gan, X.; Shang, M.; Li, Y.; Hu, Z.; Zhu, Y.; Han, L. Inorganic and Lead-Free AgBiI 4 Rudorffite for Stable Solar Cell Applications. *ACS Appl. Energy Mater.* **2018**, *1* (9), 4485– 4492, DOI: 10.1021/acsaem.8b01202
30. Pai, N.; Lu, J.; Gengenbach, T. R.; Seeber, A.; Chesman, A. S. R.; Jiang, L.; Senevirathna, D. C.; Andrews, P. C.; Bach, U.; Cheng, Y.-B.; Simonov, A. N. Silver Bismuth Sulfoiodide Solar Cells: Tuning Optoelectronic Properties by Sulfide Modification for Enhanced Photovoltaic Performance. *Adv. Energy Mater.* **2019**, *9* (5), 1803396, DOI: 10.1002/aenm.201803396
31. Tie, S.; Zhao, W.; Huang, W.; Xin, D.; Zhang, M.; Yang, Z.; Long, J.; Chen, Q.; Zheng, X.; Zhu, J.; Zhang, W.-H. Efficient X-ray Attenuation Lead-Free AgBi2I7 Halide Rudorffite Alternative for Sensitive and Stable X-ray Detection. *J. Phys. Chem. Lett.* **2020**, *11* (19), 7939– 7945, DOI: 10.1021/acs.jpclett.0c02343
32. Ye, H.; Sun, B.; Wang, Z.; Liu, Z.; Zhang, X.; Tan, X.; Shi, T.; Tang, Z.; Liao, G. High performance flexible memristors based on a lead free AgBiI 4 perovskite with an ultralow operating voltage. *J. Mater. Chem. C* **2020**, *8* (40), 14155– 14163, DOI: 10.1039/D0TC03287E
33. Grandhi, G. K.; Al-Anesi, B.; Pasanen, H.; Ali-Löytty, H.; Lahtonen, K.; Granroth, S.; Christian, N.; Matuhina, A.; Liu, M.; Berdin, A.; Pecunia, V.; Vivo, P. Enhancing the Microstructure of Perovskite-Inspired Cu-Ag-Bi-I Absorber for Efficient Indoor Photovoltaics. *Small* **2022**, *18* (35), e2203768 DOI: 10.1002/smll.202203768
34. Al-Anesi, B.; Grandhi, G. K.; Pecoraro, A.; Sugathan, V.; Viswanath, N. S. M.; Ali-Löytty, H.; Liu, M.; Ruoko, T.-P.; Lahtonen, K.; Manna, D.; Toikkonen, S.; Muñoz-García, A. B.; Pavone, M.; Vivo, P. Antimony-Bismuth Alloying: The Key to a Major Boost in the Efficiency of Lead-Free Perovskite-Inspired Photovoltaics. *Small* **2023**, e2303575 DOI: 10.1002/smll.202303575
35. Nishikubo, R.; Kanda, H.; García-Benito, I.; Molina-Ontoria, A.; Pozzi, G.; Asiri, A. M.; Nazeeruddin, M. K.; Saeki, A. Optoelectronic and Energy Level Exploration of Bismuth and Antimony-Based Materials for Lead-Free Solar Cells. *Chem. Mater.* **2020**, *32* (15), 6416– 6424, DOI: 10.1021/acs.chemmater.0c01503
36. Gray, M. B.; McClure, E. T.; Holzapfel, N. P.; Evaristo, F. P.; Windl, W.; Woodward, P. M. Exploring the AgSb1-xBixI4 phase diagram: Thermochromism in layered CdCl2-type semiconductors. *J. Solid State Chem.* **2021**, *297*, 121997, DOI: 10.1016/j.jssc.2021.121997
37. Ferro, D.; Nappi, B.; Piacente, V. Vapour pressure of antimony triiodide. *J. Chem. Thermodyn.* **1979**, *11* (2), 193– 201, DOI: 10.1016/0021-9614(79)90171-X
38. Nishikubo, R.; Kanda, H.; Garcia-Benito, I.; Molina-Ontoria, A.; Pozzi, G.; Asiri, A. M.; Nazeeruddin, M. K.; Saeki, A. Optoelectronic and energy level exploration of bismuth and antimony-based materials for lead-free solar cells. *Chem. Mater.* **2020**, *32* (15), 6416– 6424, DOI: 10.1021/acs.chemmater.0c01503
39. Chakraborty, A.; Pai, N.; Zhao, J.; Tuttle, B. R.; Simonov, A. N.; Pecunia, V. Rudorffites and Beyond: Perovskite-Inspired Silver/Copper Pnictohalides for Next-Generation Environmentally Friendly Photovoltaics and Optoelectronics. *Adv. Funct. Mater.* **2022**, *32* (36), 2203300, DOI: 10.1002/adfm.202203300
40. Luo, H.; Wu, J.; Liu, X.; Yang, Y.; Liu, Q.; Zhang, M.; Yuan, P.; Sun, W.; Lan, Z.; Lin, J. Thiourea interfacial modification for highly efficient planar perovskite solar cells. *ACS Appl. Energy Mater.* **2018**, *1* (12), 6700– 6706, DOI: 10.1021/acsaem.8b01508
41. Patil, J. V.; Mali, S. S.; Hong, C. K. A thiourea additive-based quadruple cation lead halide perovskite with an ultra-large grain size for efficient perovskite solar cells. *Nanoscale* **2019**, *11* (45), 21824– 21833, DOI: 10.1039/C9NR07377A

42. Wang, S.; Ma, Z.; Liu, B.; Wu, W.; Zhu, Y.; Ma, R.; Wang, C. High-performance perovskite solar cells with large grain-size obtained by using the Lewis acid-base adduct of thiourea. *Sol. RRL* **2018**, *2* (6), 1800034, DOI: 10.1002/solr.201800034
43. Yang, Y.; Liu, C.; Cai, M.; Liao, Y.; Ding, Y.; Ma, S.; Liu, X.; Guli, M.; Dai, S.; Nazeeruddin, M. K. Dimension-controlled growth of antimony-based perovskite-like halides for lead-free and semitransparent photovoltaics. *ACS Appl. Mater. Interfaces* **2020**, *12* (14), 17062– 17069, DOI: 10.1021/acsami.0c00681
44. Altomare, A.; Cuocci, C.; Giacovazzo, C.; Moliterni, A.; Rizzi, R.; Corriero, N.; Falcicchio, A. EXPO2013: a kit of tools for phasing crystal structures from powder data. *J. Appl. Crystallogr.* **2013**, *46* (4), 1231– 1235, DOI: 10.1107/S0021889813013113
45. Xiao, Z.; Meng, W.; Mitzi, D. B.; Yan, Y. Crystal structure of AgBi2I7 thin films. *J. Phys. Chem. Lett.* **2016**, *7* (19), 3903– 3907, DOI: 10.1021/acs.jpclett.6b01834
46. Cucco, B.; Pedesseau, L.; Katan, C.; Even, J.; Kepenekian, M.; Volonakis, G. Silver-Bismuth Halide Double Salts for Lead-Free Photovoltaics: Insights from Symmetry-Based Modeling. *Sol. RRL* **2022**, *6* (12), 2200718, DOI: 10.1002/solr.202200718
47. Mashadieva, L. F.; Aliev, Z. S.; Shevelkov, A. V.; Babanly, M. B. Experimental investigation of the Ag-Bi-I ternary system and thermodynamic properties of the ternary phases. *J. Alloys Compd.* **2013**, *551*, 512– 520, DOI: 10.1016/j.jallcom.2012.11.033
48. Kulkarni, A.; Ünlü, F.; Pant, N.; Kaur, J.; Bohr, C.; Jena, A. K.; Öz, S.; Yanagida, M.; Shirai, Y.; Ikegami, M.; Miyano, K.; Tachibana, Y.; Chakraborty, S.; Mathur, S.; Miyasaka, T. Concerted Ion Migration and Diffusion-Induced Degradation in Lead-Free Ag 3 BiI 6 Rudorffite Solar Cells under Ambient Conditions. *Sol. RRL* **2021**, *5* (8), 2100077, DOI: 10.1002/solr.202100077
49. Koedtruad, A.; Goto, M.; Amano Patino, M.; Tan, Z.; Guo, H.; Nakamura, T.; Handa, T.; Chen, W.-T.; Chuang, Y.-C.; Sheu, H.-S.; Saito, T.; Kan, D.; Kanemitsu, Y.; Wakamiya, A.; Shimakawa, Y. Structure-property relations in Ag-Bi-I compounds: potential Pb-free absorbers in solar cells. *J. Mater. Chem. A* **2019**, *7* (10), 5583– 5588, DOI: 10.1039/C8TA11227D
50. Sansom, H. C.; Whitehead, G. F. S.; Dyer, M. S.; Zanella, M.; Manning, T. D.; Pitcher, M. J.; Whittles, T. J.; Dhanak, V. R.; Alaria, J.; Claridge, J. B.AgBiI4 as a lead-free solar absorber with potential application in photovoltaics. *Chem. Mater.* **2017**, *29* (4), 1538– 1549, DOI: 10.1021/acs.chemmater.6b04135
51. Shannon, R. D. Revised effective ionic radii and systematic studies of interatomic distances in halides and chalcogenides. *Acta Crystallogr., Sect. A: Found. Adv.* **1976**, *32* (5), 751– 767, DOI: 10.1107/S0567739476001551
52. Bodenes, L.; Darwiche, A.; Monconduit, L.; Martinez, H. The Solid Electrolyte Interphase a key parameter of the high performance of Sb in sodium-ion batteries: Comparative X-ray Photoelectron Spectroscopy study of Sb/Na-ion and Sb/Li-ion batteries. *J. Power Sources* **2015**, *273*, 14– 24, DOI: 10.1016/j.jpowsour.2014.09.037
53. Merker, A.; Morgenroth, M.; Scholz, M.; Lenzer, T.; Oum, K. Critical Evaluation of the Photovoltaic Performance of (AgI) x (BiI 3) y Thin Films from the Viewpoint of Ultrafast Spectroscopy and Photocurrent Experiments. *J. Phys. Chem. C* **2023**, *127* (3), 1487– 1498, DOI: 10.1021/acs.jpcc.2c06147
54. Li, Z.; Kavanagh, S. R.; Napari, M.; Palgrave, R. G.; Abdi-Jalebi, M.; Andaji-Garmaroudi, Z.; Davies, D. W.; Laitinen, M.; Julin, J.; Isaacs, M. A.; Friend, R. H.; Scanlon, D. O.; Walsh, A.; Hoye, R. L. Z. Bandgap lowering in mixed alloys of Cs 2 Ag(Sb x Bi 1-x)Br 6 double perovskite thin films. *J. Mater. Chem. A* **2020**, *8* (41), 21780– 21788, DOI: 10.1039/D0TA07145E
55. Buizza, L. R. V.; Sansom, H. C.; Wright, A. D.; Ulatowski, A. M.; Johnston, M. B.; Snaith, H. J.; Herz, L. M. Interplay of Structure, Charge-Carrier Localization and Dynamics in Copper-Silver-Bismuth-Halide Semiconductors. *Adv. Funct. Mater.* **2022**, *32* (6), 2108392, DOI: 10.1002/adfm.202108392

56. Hooijer, R.; Weis, A.; Biewald, A.; Sirtl, M. T.; Malburg, J.; Holfeuer, R.; Thamm, S.; Amin, A. A. Y.; Righetto, M.; Hartschuh, A.; Herz, L. M.; Bein, T. Silver-Bismuth Based 2D Double Perovskites (4FPEA) 4 AgBiX 8 (X = Cl, Br, I): Highly Oriented Thin Films with Large Domain Sizes and Ultrafast Charge-Carrier Localization. *Adv. Opt. Mater.* **2022**, *10* (14), 2200354, DOI: 10.1002/adom.202200354
57. Wright, A. D.; Buizza, L. R. V.; Savill, K. J.; Longo, G.; Snaith, H. J.; Johnston, M. B.; Herz, L. M. Ultrafast Excited-State Localization in Cs2AgBiBr6 Double Perovskite. *J. Phys. Chem. Lett.* **2021**, *12* (13), 3352– 3360, DOI: 10.1021/acs.jpclett.1c00653
58. Sirtl, M. T.; Armer, M.; Reb, L. K.; Hooijer, R.; Dörflinger, P.; Scheel, M. A.; Tvingstedt, K.; Rieder, P.; Glück, N.; Pandit, P.; Roth, S. V.; Müller-Buschbaum, P.; Dyakonov, V.; Bein, T. Optoelectronic Properties of Cs 2 AgBiBr 6 Thin Films: The Influence of Precursor Stoichiometry. *ACS Appl. Energy Mater.* **2020**, *3* (12), 11597– 11609, DOI: 10.1021/acsaem.0c01308
59. Kim, Y.; Yang, Z.; Jain, A.; Voznyy, O.; Kim, G.-H.; Liu, M.; Quan, L. N.; García de Arquer, F. P.; Comin, R.; Fan, J. Z.; Sargent, E. H. Pure Cubic-Phase Hybrid Iodobismuthates AgBi2 I7 for Thin-Film Photovoltaics. *Angew. Chem., Int. Ed.* **2016**, *55* (33), 9586– 9590, DOI: 10.1002/anie.201603608
60. Zhu, H.; Erbing, A.; Wu, H.; Man, G. J.; Mukherjee, S.; Kamal, C.; Johansson, M. B.; Rensmo, H.; Odelius, M.; Johansson, E. M. J. Tuning the Bandgap in Silver Bismuth Iodide Materials by Partly Substituting Bismuth with Antimony for Improved Solar Cell Performance. *ACS Appl. Energy Mater.* **2020**, *3* (8), 7372– 7382, DOI: 10.1021/acsaem.0c00712
61. Hsiao, K.-C.; Yu, Y.-F.; Ho, C.-M.; Jao, M.-H.; Chang, Y.-H.; Chen, S.-H.; Chang, Y.-H.; Su, W.-F.; Lee, K.-M.; Wu, M.-C. Doping engineering of carrier transporting layers for ambient-air-stable lead-free rudorffite solar cells prepared by thermal-assisted doctor blade coating. *Chem. Eng. J.* **2023**, *451*, 138807, DOI: 10.1016/j.cej.2022.138807
62. Oldag, T.; Aussieker, T.; Keller, H.-L.; Preitschaft, C.; Pfitzner, A. Solvothermale Synthese und Bestimmung der Kristallstrukturen von AgBiI4 und Ag3BiI6. *Z. Anorg. Allg. Chem.* **2005**, *631* (4), 677– 682, DOI: 10.1002/zaac.200400508
63. Crovetto, A.; Hajijafarassar, A.; Hansen, O.; Seger, B.; Chorkendorff, I.; Vesborg, P. C. K. Parallel Evaluation of the BiI 3, BiOI, and Ag 3 BiI 6 Layered Photoabsorbers. *Chem. Mater.* **2020**, *32* (8), 3385– 3395, DOI: 10.1021/acs.chemmater.9b04925
64. Sansom, H. C.; Buizza, L. R. V.; Zanella, M.; Gibbon, J. T.; Pitcher, M. J.; Dyer, M. S.; Manning, T. D.; Dhanak, V. R.; Herz, L. M.; Snaith, H. J.; Claridge, J. B.; Rosseinsky, M. J. Chemical Control of the Dimensionality of the Octahedral Network of Solar Absorbers from the CuI-AgI-BiI3 Phase Space by Synthesis of 3D CuAgBiI5. *Inorg. Chem.* **2021**, *60* (23), 18154– 18167, DOI: 10.1021/acs.inorgchem.1c02773
65. Park, J. W.; Lim, Y.; Doh, K.-Y.; Jung, M. T.; Jeon, Y. in; Yang, I. S.; Choi, H.; Kim, J.; Lee, D.; Lee, W. in. Enhancement of the photovoltaic properties of Ag 2 BiI 5 by Cu doping. *Sustainable Energy Fuels* **2021**, *5* (5), 1439– 1447, DOI: 10.1039/D0SE01563F
66. Giannozzi, P.; Baroni, S.; Bonini, N.; Calandra, M.; Car, R.; Cavazzoni, C.; Ceresoli, D.; Chiarotti, G. L.; Cococcioni, M.; Dabo, I.QUANTUM ESPRESSO: a modular and open-source software project for quantum simulations of materials. *J. Phys.: Condens. Matter* **2009**, *21* (39), 395502, DOI: 10.1088/0953-8984/21/39/395502
67. Perdew, J. P.; Burke, K.; Ernzerhof, M. Generalized gradient approximation made simple. *Phys. Rev. Lett.* **1996**, *77* (18), 3865– 3868, DOI: 10.1103/physrevlett.77.3865
68. Monkhorst, H. J.; Pack, J. D. Special points for Brillouin-zone integrations. *Phys. Rev. B* **1976**, *13* (12), 5188– 5192, DOI: 10.1103/PhysRevB.13.5188
69. Grimme, S.; Antony, J.; Ehrlich, S.; Krieg, H. A consistent and accurate ab initio parametrization of density functional dispersion correction (DFT-D) for the 94 elements H-Pu. *J. Chem. Phys.* **2010**, *132* (15), 154104, DOI: 10.1063/1.3382344

70. Adamo, C.; Barone, V. Toward reliable density functional methods without adjustable parameters: The PBE0 model. *J. Chem. Phys.* **1999**, *110* (13), 6158– 6170, DOI: 10.1063/1.478522